51st AIAA Aerospace Sciences Meeting including the New Horizons Forum and Aerospace Exposition
07 - 10 January 2013, Grapevine (Dallas/Ft. Worth Region), Texas

AIAA 2013-0786

Results using NSU3D for the First Aeroelastic Prediction Workshop

Dimitri J. Mavriplis * Zhi Yang † Michael Long ‡ Jay Sitaraman §
Department of Mechanical Engineering, University of Wyoming, Laramie, WY 82071

This paper details the results obtained with the NSU3D unstructured mesh Reynolds-averaged Navier-Stokes solver for the first Aeroelastic Prediction Workshop. Three different test cases were computed for the workshop: The Rectangular Supercritical Wing (RSW) case, the Benchmark Supercritical Wing case (BSCW), and the High-Reynolds Number Aero-Structural Dynamics (HIRENASD) test case. Results are shown for all three test cases using different grid sizes, time step sizes and in some cases convergence criteria. Computational results are compared with experimental data and are also assessed for grid convergence and temporal convergence.

I. Introduction

The community workshop model for assessing the state-of-the-art in computational methods for aerospace engineering has gained popularity over the last decade. This has been due largely to the success of the Drag Prediction Workshop (DPW) series, which initiated its first workshop in June 2001,[1] and recently completed its fifth workshop in June 2012.[2] The principal focus of the DPW series has been the prediction of forces and moments for steady-state aircraft cruise conditions. Over the years, this success has been replicated in other workshops devoted either to studying more specific flow phenomena such as the Shock-Boundary-Layer Workshop,[3] or focused on more complex aerodynamic problems, such as the High-Lift Prediction Workshop series.[4] The Aeroelastic Prediction Workshop (AePW) represents the latest incarnation of this community workshop model, targeting the assessment of numerical methods for simulating aeroelastic problems. This represents a substantial increase in complexity compared to previous workshops, due to the fact that aeroelasticity problems are inherently both time-dependent and multidisciplinary. For example, while the DPW series has been able to focus on quantifying spatial discretization error, the AePW series must also include the effect of temporal disrecretization errors and algebraic errors due to incomplete convergence at each implicit time step. Additionally, errors in the structural dynamics model and the fluid-structure coupling will certainly play a role in overall simulation accuracy and must be considered as well. In order to assess these various error sources, a methodical approach to studying their individual effects is warranted before moving on to the fully coupled problem. Thus, the first AePW was intentionally designed to focus on problems that stress the unsteady aerodynamic prediction component of the overall aeroelastic problem while minimizing the importance of the structural dynamics and aeroelastic coupling components. With this in mind, three aeroelastic benchmark test cases were chosen for the workshop: the first two consisting of a rigid transonic wing undergoing a prescribed periodic pitching motion, an the third test case consisting of a weakly coupled aeroelastic transonic wing which could be simulated using linear modal analysis. These three test cases were intended to form a suite of progressively more difficult simulation benchmarks for which experimental data is available for comparison.

The first AePW was held in April 2012, prior to the AIAA 53rd Structures, Structural Dynamics and Materials Conference in Honolulu, HI. The stated objectives of the workshop were to provide an impartial forum for the assessment of the state-of-the-art in Computational Aeroelasticity(CAe) methods as practical tools for the prediction of static and dynamic aeroelastic phenomena and responses on relevant geometries,

*Professor, AIAA Associate Fellow; email: mavriplis@uwyo.edu
†Research Scientist, AIAA member; email: zyang@uwyo.edu
‡Application Engineer, AIAA member; email:mikelong@scientific-sims.com
§Assistant Professor, AIAA member; email jsitaram@uwyo.edu

including identifying gaps in existing aeroelastic databases, identifying errors and uncertainties in computational methods, and providing a roadmap for future research. Overall, 17 analysis teams from 10 nations provided a total of 26 analysis datasets. This paper describes the results of one of those analysis teams using the NSU3D flow solver applied to all three test cases.

The NSU3D code has been a participant in all five DPW workshops since 2001,[5–8] as well as the first High-Lift prediction workshop held in 2010.[9] NSU3D has also been involved in various DPW follow-on studies, including comparisons with other solvers,[6] sensitivity studies, and extensive grid refinement studies.[10] NSU3D also is currently used as a near-body unstructured mesh solver component within the HELIOS comprehensive rotorcraft simulation software, where it is used for the simulation of time-dependent aerodynamic and aeroelastic rotorcraft relevant problems.[11]

The NSU3D solver is described briefly in the next section along with the other software components required for aeroelastic simulations such as mesh deformation and available structural models. In the subsequent sections, each AePW test case is first described, followed by the results obtained using the aforementioned software. The final section provides a summary an outlook of future work.

II. Solver Description

The NSU3D code is an unstructured mesh multigrid Reynolds-averaged Navier-Stokes (RANS) solver for high-Reynolds number external aerodynamic applications. The NSU3D discretization employs a vertex-based approach, where the unknown fluid and turbulence variables are stored at the vertices of the mesh, and fluxes are computed on faces delimiting dual control volumes, with each dual face being associated with a mesh edge. This discretization operates on hybrid mixed-element meshes, generally employing prismatic elements in highly stretched boundary layer regions, and tetrahedral elements in isotropic regions of the mesh away from the aircraft surfaces. A single edge-based data-structure is used to compute flux balances across all types of elements. The convective terms are discretized as central differences with added matrix dissipation. Second-order accuracy is achieved by formulating these dissipative terms as an undivided biharmonic operator, which is constructed in two passes of a nearest-neighbor Laplacian operator. In the matrix form, this dissipation is similar to that produced by a Riemann solver gradient-based reconstruction scheme, and is obtained by replacing the difference in the reconstructed states on each side of the control volume interface by the undivided differences along mesh edges resulting from the biharmonic operator construction. These differences are then multiplied by the characteristic matrix to obtain the final dissipation terms. A Roe upwind scheme using least-squares gradient reconstruction is also available in the NSU3D solver.

The baseline NSU3D discretization employs a finite-difference scheme to approximate the thin-layer form of the viscous terms for the Navier-Stokes equations, although this is done in a multidimensional fashion, by computing a Laplacian of the velocity field.[12] The main approximation in this approach is the omission of the cross-derivative viscous terms, and the assumption of a locally constant viscosity. The discretization of the full Navier-Stokes terms based on a hybrid gradient-of-gradient approach is also available, where the second derivatives in the directions aligned with the incident mesh edges are computed using a nearest-neighbor stencil.

NSU3D incorporates the single equation Spalart-Allmaras turbulence model,[13] as well as a standard $k-\omega$ two-equation turbulence model,[14] and the two-equation shear-stress transport (SST) model due to Menter.[15] For the workshop simulations, the Spalart-Allmaras turbulence model was used exclusively.

Various temporal discretizations are incorporated, including first, second and third-order backwards Euler discretizations (BDF1, BDF2, BDF3) and a suite of diagonally implicit Runge-Kutta schemes. For the purposes of the AePW workshop calculations, the BDF2 scheme was used exclusively.

Grid speed terms are implemented in order to handle dynamically deforming mesh cases. These are formulated as control-volume face-integrated values constructed from differences in grid coordinates at successive time instances. The particular formulation satisfies the geometric conservation law exactly for all implemented time-stepping schemes, thus guaranteeing discrete conservation for dynamic mesh simulations.[16]

The non-linear system arising at each implicit time step is solved iteratively using a non-linear line-preconditioned agglomeration multigrid algorithm. This solver is formed by invoking the non-linear steady-state multigrid solver in a dual pseudo-time stepping mode. Coarse multigrid levels are formed using a graph algorithm in a preprocessing stage, and an implicit line solver is used in regions of high mesh stretching (i.e. boundary layer regions) on each multigrid level for faster convergence. A linear line-implicit multigrid algorithm is also available and can be used to solve the linear system within each step in a Newton method

applied to the non-linear system arising at each implicit time step.

More recently, NSU3D has been extended for use in coupled aeroelastic calculations. In reference,[17] a structural analysis modal model was implemented in conjunction with the NSU3D solver and used to solve the AGARD 445.6 aeroelastic test case.[18] In addition to the implementation of the modal model, a highly scalable Euler-Bernoulli slender beam model suitable for large aspect ratio structures (e.g. transport aircraft wing, helicopter rotor blades) has been developed and coupled with NSU3D. Computations using this beam structural model have been documented in references.[19–21]

Considerable work has focused on the development of a robust and efficient mesh deformation technique.[17,22] The developed approach is based on a linear elasticity model with optimally prescribed mesh stiffness for added robustness. The mesh deformation equations are solved using a line-implicit multigrid algorithm similar to the solver used in the CFD code, resulting in good scalability and rapid convergence of the mesh motion equations.

III. Rectangular Supercritical Wing Test Case

1. Test Case Description

The Rectangular Supercritical Wing (RSW) is a rigid unswept wing of aspect ratio 2 that was tested in the Transonic Dynamics Tunnel (TDT) at NASA Langley in 1983.[23] The wing root was mounted on a turntable located at the wind tunnel wall in order to enable periodic pitching of the wing about its 45% chord location as shown in Figure 1(a). Experiments were conducted at pitching frequencies of 0 Hz (i.e. steady), 10 Hz and 20 Hz using heavy gas (R-12) as the test fluid medium. Time-dependent pressure measurements were taken at four span locations ($y/b = 0.308, 0.588, 0.809$, and 0.951) and were available for comparison with computational results. The RSW was conceived as an entry-level unsteady transonic aerodynamic test case since the geometry and flow conditions were expected to result in relatively benign flow phenomena. In order to mitigate the effects of the wind-tunnel wall boundary layer, the model was mounted on a splitter plate which provided a 6" offset from the wind tunnel wall. During the organization of the workshop, preliminary calculations were performed to assess the impact of the splitter plate.[24] It was found that the wind-tunnel wall boundary layer was approximately 12" thick at the model location, and hence the splitter plate was unintentionally immersed in the boundary layer. Thus the impact of the wind-tunnel wall boundary layer could not be neglected, making this test case considerably more difficult than intended. However, it was also determined that modeling the test geometry as a simple wing extruded to the wall (an additional 6" span) in the absence of the splitter plate produced nearly identical results to modeling the considerably more complex complete wing, splitter-plate, wind-tunnel wall configuration. Thus the simulations performed in this work employed a 55" span wing attached perpendicularly to a no-slip wall. One difficulty with this configuration is that the no-slip wall could no longer be moved as the wing is pitched, as would be the case if the entire grid were pitched as a solid body. Thus, a circular patch on the wind tunnel wall was defined and enforced to rotate with the pitching wing, while the remaining portion of the wall was held fixed, as shown in Figure 1(b). The computational mesh was then deformed as required during the pitching motion by allowing a small mesh transition region between the moving patch boundary and fixed wind tunnel wall region. While this setup is inexact, (for example it induces wall velocities on the rotating patch as shown in Figure 1(c)) it represents an approximation to the wind-tunnel wall turntable used to pitch the wing.

2. Computational Results

All simulations were performed using a ratio of specific heats ($\gamma = 1.132$) representative of R-12 heavy gas. It should be noted that this change in γ from the nominal value for air of 1.4 has a significant effect on the results, for example producing changes of the order of 5% to 10% in CL values at the nominal steady state transonic conditions. Both steady and time dependent simulations were performed. For all cases, the Mach number was 0.825 and the Reynolds number was 4.01 million, while the two steady-state cases used angles of attack of 2^o and 4^o, and the two time-dependent cases used the same mean incidence of 2^o but two different pitching frequencies of $10Hz$ and $20Hz$ with an amplitude of 1^o.

Three different meshes were used for these cases, a coarse, medium and fine mesh, containing 2,878,627, 7,072,791, and 18,277,610 mesh points, respectively. These meshes correspond to the 55 inch wing span geometry, where the wing was extended to the wind-tunnel wall in the absence of the splitter plate. They are all self-similar hybrid prismatic-tetrahedral unstructured meshes generated using SOLID MESH, sup-

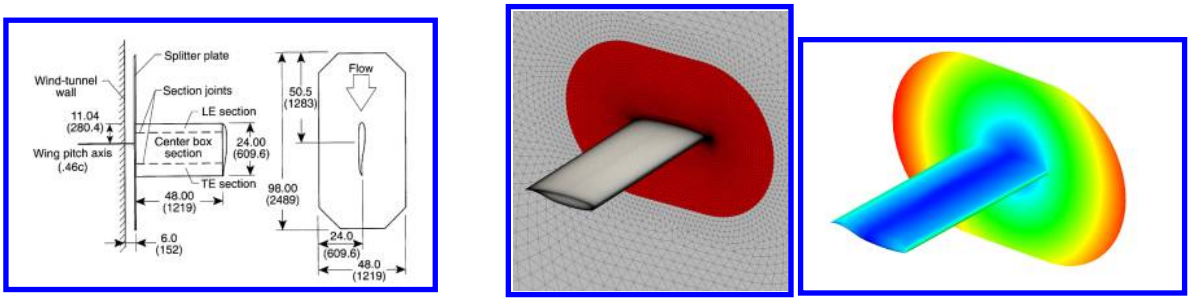

(a) Geometry definition (b) Coarse mesh (c) Surface velocities

Figure 1. Rectangular Supercritical Wing (RSW) geometry definition (a) and grid patching system (b) with induced surface velocities from pitching motion (c).

plied by the workshop organizing committee and labeled *rsw_coarse_mixed_nc*, *rsw_medium_mixed_nc*, and *rsw_fine_mixed_nc*, respectively. While all three meshes were used for the steady-state cases, only the coarse and medium meshes were used for the time-dependent cases, due to resource constraints.

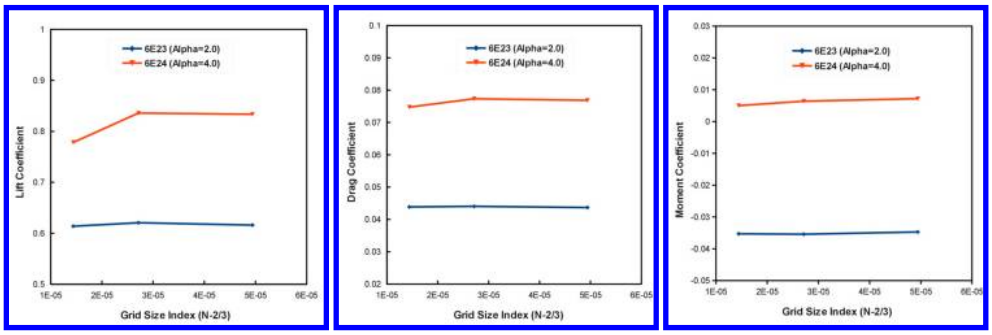

Figure 2. Grid Convergence for steady-state RSW test cases

.

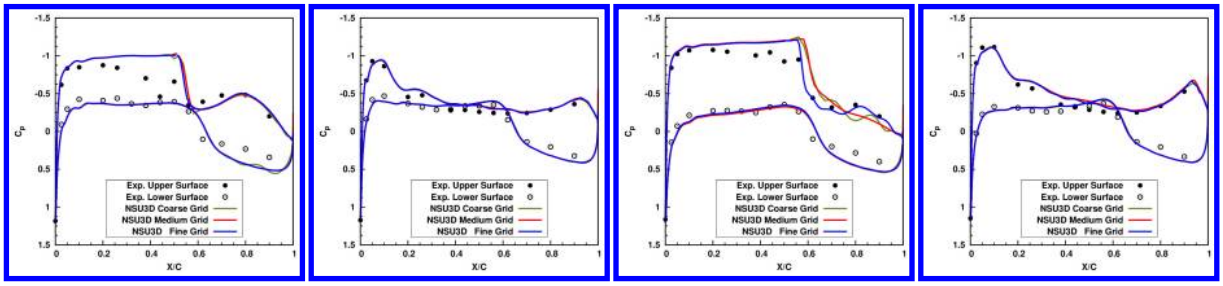

(a) Incidence=2^o, y/b=0.309 (b) Incidence=2^o, y/b=0.951 (c) Incidence=4^o, y/b=0.309 (d) Incidence=4^o, y/b=0.951

Figure 3. Comparison of computed and experimental steady surface pressures for RSW case.

Figure 2 depicts the grid convergence of lift, drag and pitching moment for both steady-state cases showing reasonable grid convergence, although the C_L value for the 4^o angle of attack case appears to be dropping more rapidly between the medium and fine grids. Figures 3 illustrate the steady wing surface pressure distributions at the four span stations. The most notable aspect of these results is the discrepancy in the computed versus experimental shock location at the inboard station which vanishes at the outboard station. This was noted in the collective workshop results and is attributed to the effect of the wind-tunnel wall boundary layer. However, a measurement of the wall boundary layer produced by NSU3D at the same downstream location as the model is in agreement with that predicted by other codes and experimentally. A possible explanation may be interference effects between the wing aerodynamics and the wall velocities

imposed by the rotating patch as shown in Figure 1. However, the precise interaction between the wall boundary layer and the transonic shock location remains to be investigated in more detail.

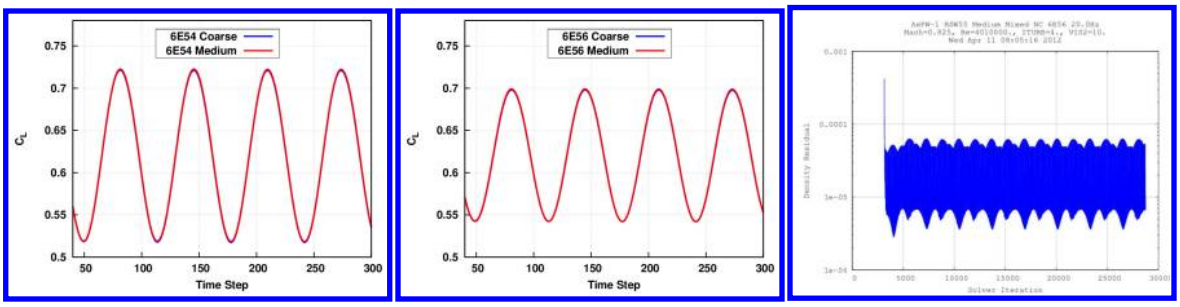

(a) (b) (c)

Figure 4. Time dependent lift coefficient histories at (a) f=10Hz, and (b) f=20Hz; (c) Convergence history at each implicit time step for f=20Hz case.

The time-dependent simulations were performed for the f=10Hz and f=20Hz cases using the coarse and medium grids. For all cases, 64 time steps per period were used and each implicit time step was solved using 50 line-implicit multigrid cycles. These simulations required approximately 0.45 secs/cycle and 0.68 secs/cycle for the coarse and fine grids running on 128 and 256 Intel Sandybridge cores respectively for a total simulation time of 24 minutes and 36 minutes per period for the coarse and fine meshes on 128 and 256 cores. While a full time step convergence study was not performed on these cases, preliminary investigations over small numbers of time steps were used to establish independence of the overall time-dependent forces to the chosen time step size and level of convergence.

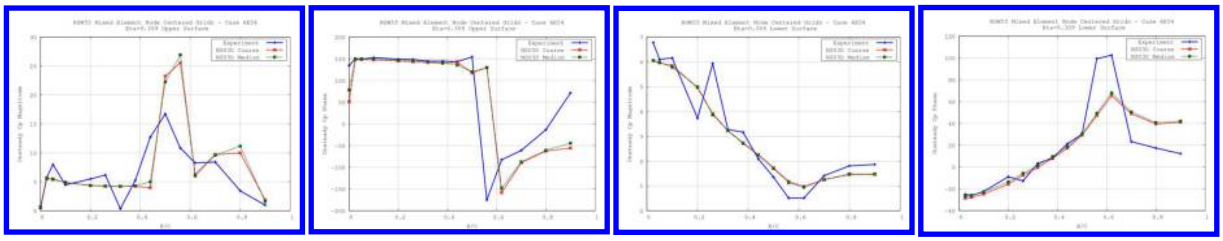

(a) Magnitude upper surface (b) Phase upper surface (c) Magnitude lower surface (d) Phase lower surface

Figure 5. Magnitude and phase of unsteady pressure fluctuations at y/b=0.309 span location for RSW test case at f=10Hz

.

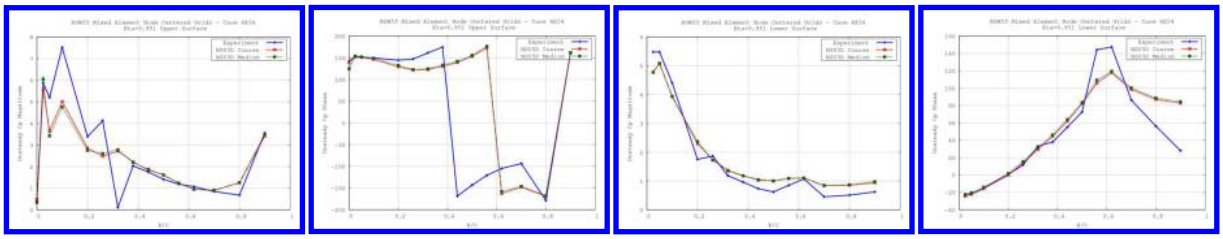

(a) Magnitude upper surface (b) Phase upper surface (c) Magnitude lower surface (d) Phase lower surface

Figure 6. Magnitude and phase of unsteady pressure fluctuations at y/b=0.588 span location for RSW test case at f=10Hz

.

The computed time dependent pitching moment coefficient is shown in Figure 4 for both f=10Hz and f=20Hz cases showing relatively benign characteristics and relatively little changes between the coarse and medium grids. The time-dependent convergence history is also shown in Figure 4(c) where each implicit time step is seen to be converged by approximately 1.5 orders of magnitude, resulting in well converged force

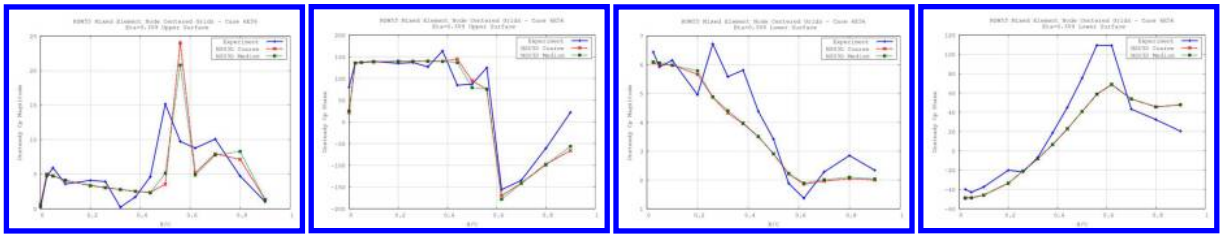

(a) Magnitude upper surface (b) Phase upper surface (c) Magnitude lower surface (d) Phase lower surface

Figure 7. Magnitude and phase of unsteady pressure fluctuations at y/b=0.809 span location for RSW test case at f=20Hz

.

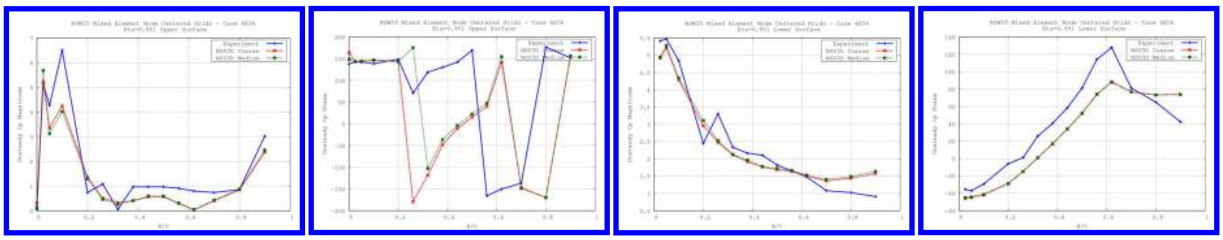

(a) Magnitude upper surface (b) Phase upper surface (c) Magnitude lower surface (d) Phase lower surface

Figure 8. Magnitude and phase of unsteady pressure fluctuations at y/b=0.951 span location for RSW test case at f=20Hz

.

values at each time step. The computed periodic time-dependent surface pressures were postprocessed by extracting the magnitude and phase (or real (in phase) and imaginary (out-of-phase)) components of the pressure variations at the frequency of the forced pitching motion and comparing these with experimental values. These comparisons are shown in Figures 5 through 8 for all four stations for both f=10Hz and f=20Hz cases. The agreement with experiment follows the pattern observed in the steady-state cases, with the largest discrepancies being attributed to the inboard shock location as affected by the wind-tunnel wall boundary layer. In the outboard span regions, good agreement with experimental values is observed particularly for the magnitude values, although larger discrepancies in the phase angle on the upper surface remain at the outermost station.

IV. Benchmark Supercritical Wing Test Case

3. Test Case Description

The Benchmark Supercritical Wing (BSCW) also consists of a rectangular wing of aspect ratio 2, but uses a different airfoil shape (NASA SC(2)-0414) than the RSW, as shown in Figure 9. The experimental setup is similar to the RSW, involving a rigid wing undergoing forced pitching motion about its 30% chord location, but operates at a higher Mach number and incidence, thus producing more non-linear and challenging flow phenomena including shock-induced separation. The BSCW was also tested in the NASA Langley TDT and used a newer mounting mechanism with splitter plate that placed the model well outside of the wind-tunnel wall boundary layer, as seen in Figure 9(b). This not only avoids the difficulties encountered with the boundary layer influence in the RSW case, but enables the wall to be treated as a symmetry plane or inviscid slip wall, which in turn makes it possible to model the pitching wing by rotating the entire grid as a solid body, since the motion of the inviscid wall will not be felt by the flow. Additionally, the BSCW was tested using R-134a heavy gas (after the conversion of the TDT from R-12 to R134a), and thus all computations were performed using the value of $\gamma = 1.116$ for R134a gas. Three different BSCW test cases were considered, a steady case (f=0Hz) at a nominal angle of attack of 5^o, and two time-dependent cases at the same mean angle of attack (5^o) but with a 1^o amplitude pitching motion at either f=1Hz or f=10Hz. In all cases, the freestream Mach number was 0.85 and the Reynolds number was 4.491 million. The experimental BSCW

data set contains only a single row of pressure measurements located at the 60% span location.

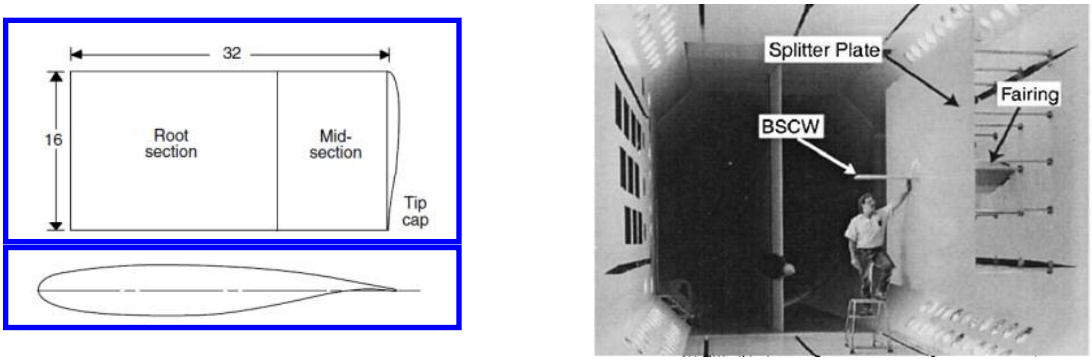

(a) (b)

Figure 9. Benchmark Supercritical Wing (BSCW) geometry definition

4. Computational Results

All cases for the BSCW were run using two meshes, namely the coarse and medium resolution unstructured hybrid (prismatic-tetrahedral) meshes supplied by the workshop organizing committee labeled *bscw_coarse_mixed_nc* and *bscw_medium_mixed_nc*. These meshes were generated using the VGRID software package and constructed as a family of self-similar meshes suitable for a grid convergence study and contained 2,968,550 and 9,005,346 points respectively. Convergence histories for the steady-state case (Mach=0.85, Incidence = 5^o) on both grids are shown in Figure 10. Although the coarse mesh converges robustly, the medium mesh fails to converge fully to a steady result with small oscillations remaining in the force histories. Subsequently, the medium mesh case was rerun in time dependent mode and still failed to produce a steady result for a range of time step sizes. This behavior is attributed to the onset of unsteady flow phenomena for the BSCW at these conditions. Interestingly, this behavior persists in the low frequency (f=1Hz) time-dependent periodic pitching case but disappears for the higher frequency (f=10Hz) pitching case as will be seen in the description of these cases below.

For the two time-dependent forced pitching cases, both the coarse and medium meshes were run in order to provide a rudimentary grid convergence study. In addition, a range of time step sizes were used and a number of different sub-iterations per time step were employed in order to study the effect of temporal error and algebraic (incomplete convergence) error on the computed results.

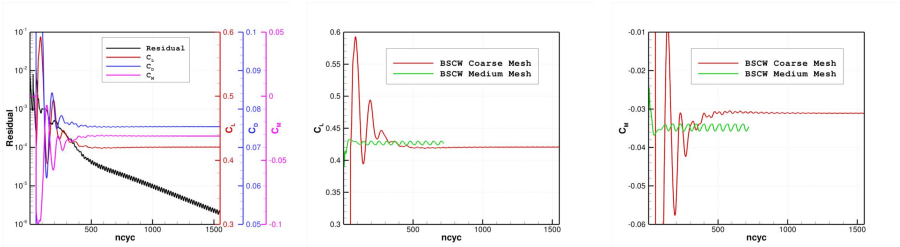

(a) Coarse mesh (b) Coarse and fine mesh CL (c) Coarse and fine mesh CM

Figure 10. Steady-state convergence histories for coarse and medium meshes for BSCW test case.

Figure 11 depicts the force coefficient time histories computed for the f=1Hz case using 180, 360 and 720 time steps per period, with 20 or 50 multigrid sub-iterations per time step on the coarse grid, and using 720 time steps per period with 50 multigrid subiterations per time step on the medium grid. Although the lift coefficient time history shows only minor variations with time-step, subiteration and mesh size, the drag coefficient shows appreciable variations, and the pitching moment coefficient histories show larger differences

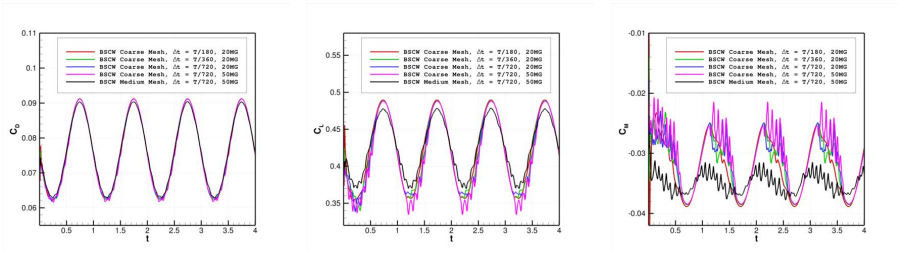

(a) Lift coefficient (b) Drag coefficient (c) Pitching moment

Figure 11. Computed time-dependent force and moment histories for BSCW test case at f=1Hz.

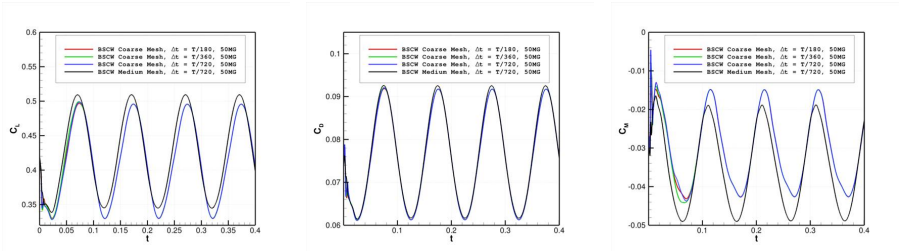

(a) Lift coefficient (b) Drag coefficient (c) Pitching moment

Figure 12. Computed time-dependent force and moment histories for BSCW test case at f=10Hz.

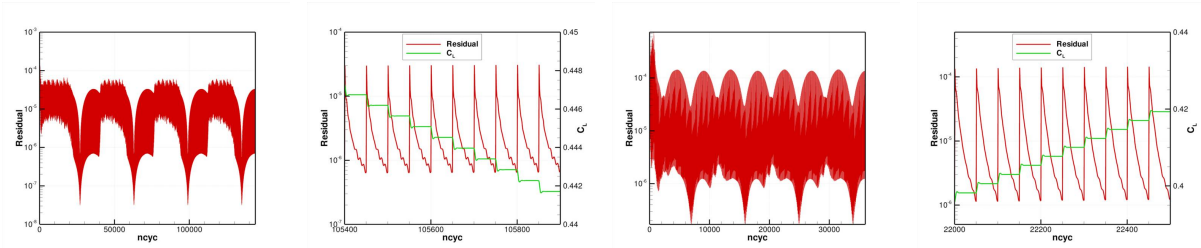

(a) f=1Hz (Global view) (b) f=1Hz (Detailed view) (c) f=10Hz (Global view) (d) f=10Hz, (Detailed view)

Figure 13. Convergence history for BSCW case at f=1Hz and f=10Hz using 720 time steps per period.

indicative of a lack of spatial (grid) and temporal (time-step) convergence. The situation is much different for the f=10Hz simulations shown in Figure 12. All force and moment time histories show little sensitivity to the time step size and number of subiterations, although some variation in the moment time histories between the coarse and fine grids remains. These results, combined with the convergence difficulties encountered for the steady-state case, point to a fundamental instability in the mean flow for the BSCW at these conditions that operates at a frequency that is higher than the f=1Hz pitching motion, but lower than the f=10Hz pitching motion. For example, comparing the simulations using 180 time steps per period of the f=1Hz and f=10Hz cases, the physical time step for the latter run is 10 times smaller than that for the former case, and thus better able to resolve any underlying instability that is not related to the pitching motion. This is further demonstrated in the time-dependent convergence plots shown in Figure 13 for both f=1Hz and f=10Hz cases. In the low frequency case, the implicit system at each time step is seen to converge by only one order of magnitude although the lift coefficient seems well converged at each time step. However, looking at the convergence histories over all time steps reveals regions within the 1Hz periodic motion where overall convergence is substantially less than one order of magnitude using a constant 50 multigrid cycles per time step. On the other hand, the non-linear system at each time step is reduced by over 2 orders of magnitude at each time step for the f=10Hz case, as shown in Figure 13 and there is much less variation in the level of attained convergence at each time step throughout the entire simulation. These results provide an illustration of the requirement of resolving the important physical time scales in a time dependent simulation.

Figure 14 provides a comparison of the mean computed and experimental surface pressures at the 60% span location for the steady and low and high frequency pitching cases. In spite of the convergence difficulties and sensitivities to time-step, convergence and mesh sizes, the mean pressures for all cases display remarkably little variation and reasonable agreement with experimental values except in the aft portion of the airfoil where the pressure coefficient values are overpredicted. This overprediction was seen also in the collective workshop results.[24]

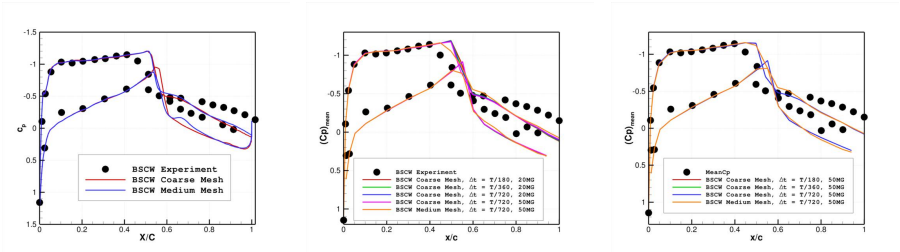

(a) Steady (f=0Hz) (b) f=1Hz (c) f=10Hz

Figure 14. Comparison of computed and experimental steady/mean pressures for BSCW case

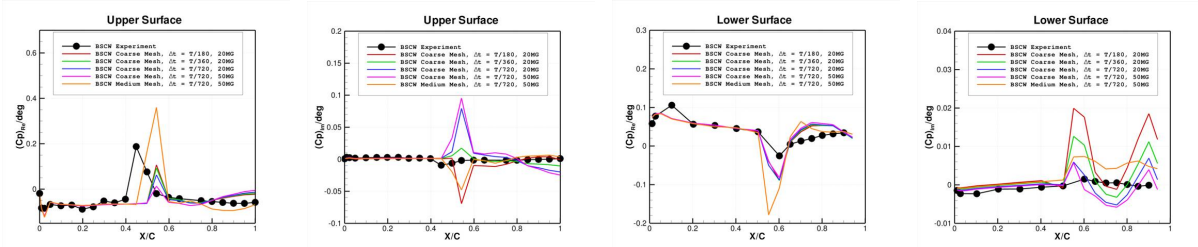

(a) Real upper surface (b) Imaginary upper surface (c) Real lower surface (d) Imaginary lower surface

Figure 15. Comparison of computed and experimental real and imaginary pressure fluctuations for BSCW case at f=1Hz.

The real (in phase) and imaginary (out of phase) pressure fluctuations at the pitching frequency (normalized by the pitching amplitude) are plotted for the f=1Hz case in Figure 15 and for the f=10Hz case in Figure 16. For the workshop, pressure fluctuations were postprocessed as mean and phase as well as real and imaginary components, and are shown in the latter format here for clarity. The computed results reproduce the general trends of the experimental data although some discrepancies due to shock location are apparent

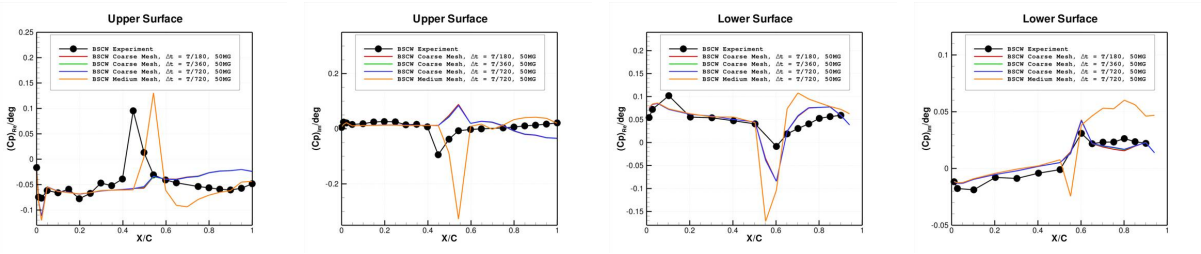

(a) Real upper surface (b) Imaginary upper surface (c) Real lower surface (d) Imaginary lower surface

Figure 16. Comparison of computed and experimental real and imaginary pressure fluctuations for BSCW case at f=10Hz.

for both low and high frequency cases. As expected, the f=1Hz results show more sensitivity to the time step size and convergence criteria, while both f=1Hz and f=10Hz show some sensitivity to the mesh size, particularly for the imaginary component on the lower surface. This indicates that spatial discretization error remains appreciable in these cases and results using finer meshes will be required to further investigate grid sensitivity.

V. High Reynolds Number Structural Dynamics Model

5. Test Case Description

The High Reynolds Number Aero-Structural Dynamics (HIRENASD) model was chosen as an initial coupled aeroelastic analysis test case. The basic configuration consists of a 34^o swept wing model with with a BAC 3-11 supercritical airfoil profile as shown in Figure 17. This configuration was tested in the ETW as a semi-span model ceiling-mounted through a non-contacting fuselage fairing to a turntable, balance and excitation system. The model and balance were designed to be very stiff, with well-separated modes. The first two wing bending modes have frequencies of approximately 27 and 78.9 Hz and the first wing torsion mode has a frequency of approximately 265 Hz. The model instrumentation includes unsteady pressure transducers at 7 span stations. In addition to the unsteady pressures, balance measurements and accelerations were obtained. For a small set of data points, wing displacements were also extracted via stereo pattern tracking. Experimental results and associated computational studies for the HIRENASD model have previously been published.[25,26] For the workshop, steady-state and time-dependent analyses at two different Mach numbers, two different incidences, and two different Reynolds numbers were suggested. In the current work, only one steady-state condition and the corresponding time-dependent test condition have been simulated. For these cases, the Mach number was 0.8, the Reynolds number was 7 million, and the incidence was 1.5 degrees. Because the wing is flexible, the steady-state case must include aeroelastic effects. For the time-dependent case, the wing was excited in its second bending mode by a differential forcing applied at the wing root at the resonant frequency (78.9Hz). The modal shapes of the wing were provided by the workshop organizing committee and could be used directly to simulate this motion through prescribed modal oscillations at the measured amplitude, since the aeroelastic coupling was assumed to be relatively weak. Alternatively, using a suitable structural model, the experimental forcing could be prescribed and the coupled aeroelastic problem solved. The test medium was nitrogen, and therefore the value $\gamma = 1.4$ was used in all simulations.

6. Computational Results

The steady-state and time-dependent cases at Mach=0.8, Re=7 million and Incidence = 1.5^o were computed using the coarse and medium hybrid unstructured meshes generated using the VGRID software package and supplied by the workshop organizing committee labeled *coarse_mixed_nc* and *medium_mixed_nc*. The coarse mesh contained a total of 6,361,743 points and the medium mesh contained 19,061,710 mesh points. For the steady-state case, a static aeroelastic simulation was performed using the first 20 modes of the structural model. Figure 18(a) illustrates the convergence for this case on the coarse mesh, including the convergence of the modes in the structural solver in Figure 18(b). The aeroelastic deflection is plotted along the span in Figure 18(c), while the pressure distributions at four different span locations are shown in Figure 19 for the

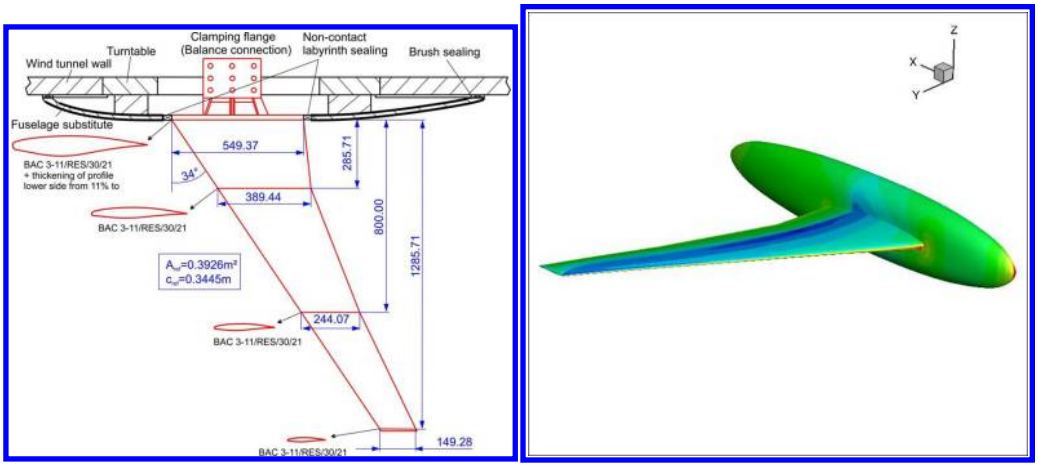

(a) (b)

Figure 17. (a) HIRENASD geometry definition; (b) Computed surface pressure distribution for Mach=0.8, Incidence = 1.5^o, Re = 7 million

.

steady rigid and steady aeroelastic cases, showing small but increasing differences due to the static aeroelastic effects as one proceeds towards the outboard stations. Figure 20 provides a comparison of the computed surface pressures at these same span locations between the coarse and fine meshes showing differences mostly confined to the upper surface shock location and resolution. Table 1 depicts the computed force coefficient values for the rigid configuration and the static aeroelastic configuration for both mesh sizes, which are in good agreement with the collective workshop results.[24]

Table 1. Computed force and moment coefficients for rigid and steady aeroelastic cases.

	CL	CD	CM
Coarse Mesh, Rigid	0.35482	0.01419	-0.29435
Coarse Mesh, Aeroelastic	0.33678	0.01353	-0.27697
Medium Mesh, Rigid	0.35280	0.01382	-0.29346
Medium Mesh, Aeroelastic	0.33486	0.01315	-0.27618

The time-dependent case was first simulated as a prescribed motion problem. The prescribed motion was obtained by applying a periodically varying amplitude to the second bending mode shape of the wing, projected onto the surface grid for the CFD computation. The amplitude was scaled to match the measured amplitude near the wing tip of 2.4 mm and the frequency of the motion was taken as 78.9 Hz. At each time step, the prescribed deflections were first applied to the surface mesh, and the interior mesh was then deformed using the linear elastic mesh motion approach, followed by the implicit solution of the time-dependent flow RANS equations. Figure 21 illustrates the convergence of the flow solver at each implicit time step showing a 1.5 to 2 order reduction in the residual over 50 sub-iterations with good convergence of the lift coefficient within each time step. The computed time histories of lift, drag and pitching moment coefficients are shown for both grid sizes in Figure 22 showing relatively smooth variations in time and some variation with grid size. Figures 23 through 29 depict the real and imaginary components of the pressure fluctuations divided by the modal amplitude at the second-bending mode natural frequency (forcing frequency) on the wing at the various spanwise stations. Agreement with experimental values is generally good with some discrepancy in the fluctuating shock location, and overprediction of the pressure fluctuations aft of the shock, particularly at the outer span stations. Lower surface fluctuating pressures are generally in good agreement with experimental values. The numerical simulations are shown for both mesh sizes in all cases. In general, the upper surface results show some grid sensitivity particularly in the shock region, while the lower surface results appear to be relatively grid converged. It should be noted that repeating these

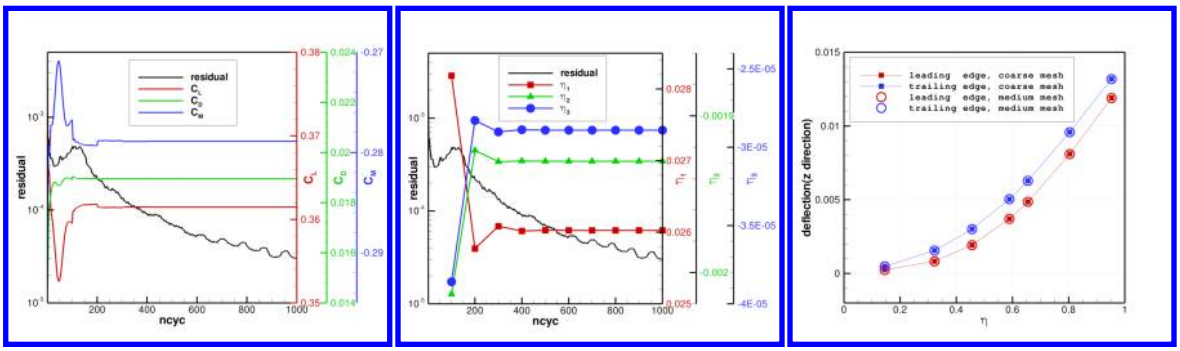

(a) Convergence history (b) Modal convergence history (c) Static aeroelastic deflection

Figure 18. Steady-state aeroelastic (a) residual and force convergence history (b) structural modal convergence, and (c) static aeroelastic spanwise wing deflection for HIRENASD test case at Mach=0.8, Incidence = 1.5^o, Re=7 million.

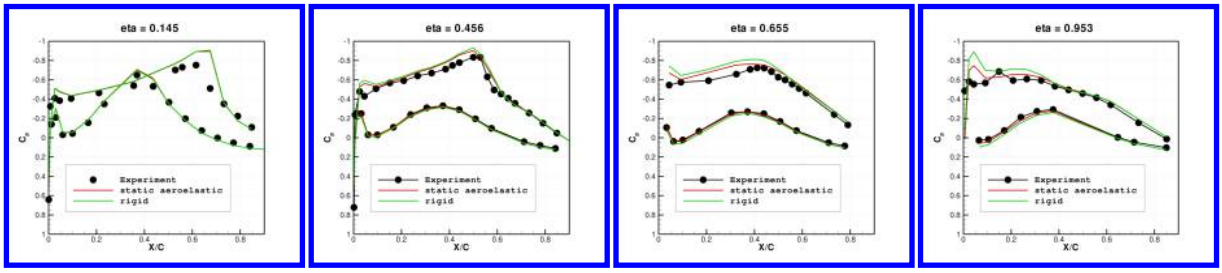

Figure 19. Comparison of rigid and static aeroelastic surface pressure distributions on coarse mesh at various span stations.

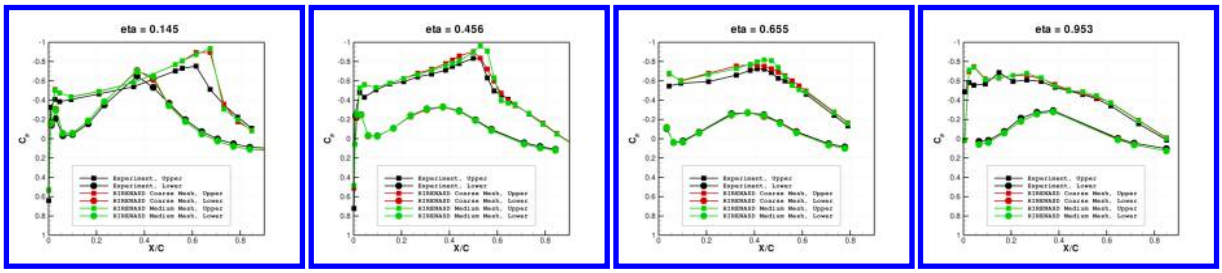

Figure 20. Comparison of static aeroelastic surface pressure distributions on coarse mesh and fine mesh with experimental data at various span stations.

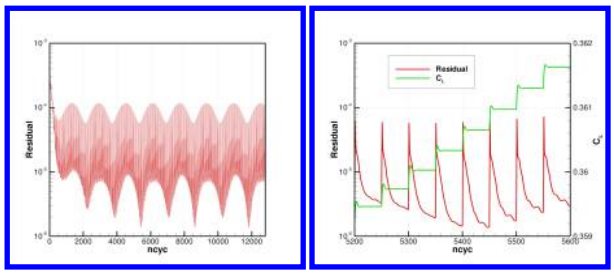

(a) (b)

Figure 21. Time-dependent convergence history for HIRENASD test case with prescribed motion second-bending mode deflection at 78.9Hz on coarse mesh using 64 time steps per period; (a) Global history, (b) detailed view over several time steps.

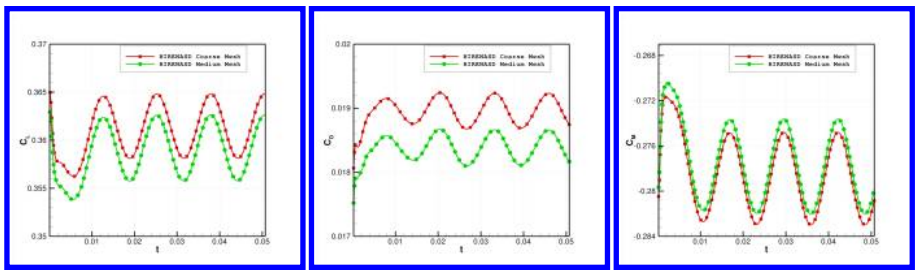

(a) (b) (c)

Figure 22. Computed time-dependent (a) lift, (b) drag, and (c) moment histories for HIRENASD with prescribed motion second-bending mode deflection at 78.9Hz.

simulations at higher modal amplitudes produced essentially identical results, pointing to a relatively linear response in this regime.

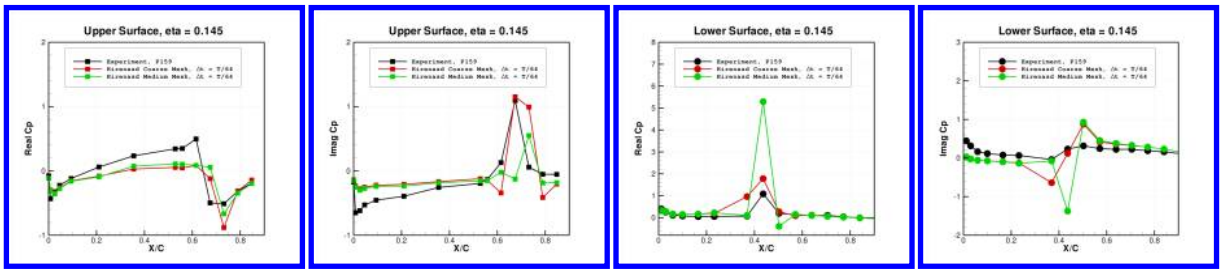

Figure 23. Comparison of computed versus experimental real and imaginary pressure fluctuations at y/b=0.145 station for HIRENASD with prescribed motion second-bending mode deflection at 78.9Hz.

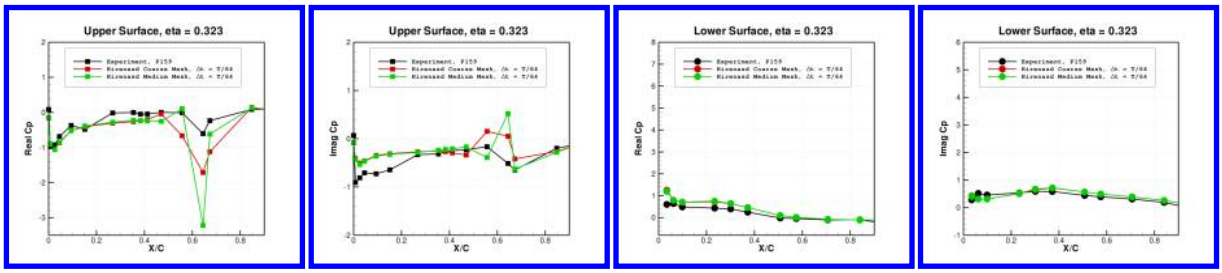

Figure 24. Comparison of computed versus experimental real and imaginary pressure fluctuations at y/b=0.323 station for HIRENASD with prescribed motion second-bending mode deflection at 78.9Hz.

In order to perform a fully coupled aeroelastic simulation, a beam model was constructed and calibrated to the published modal shapes and frequencies of the HIRENASD model. The beam model was cantilevered at the root, and positioned along the quarter chord location of the swept wing. The model consisted of 512 bend-twist beam elements and the stiffnesses were prescribed through an optimization procedure that sought to match the modal shapes and frequencies of the first 5 structural modes. Figure 30 illustrates the location of the beam model for the coupled aeroelastic simulations and a snapshot of the instantaneous computed surface pressures including an inset of overall beam deflection time history. The coupled aeroelastic results utilizing the beam model were only performed for a single time step size (64 per period) on the medium mesh (6 million points). The time history of the force coefficients for this case was compared with that obtained using the prescribed modal deflections, and good agreement was observed. Figure 31 provides a comparison of the fluctuating surface pressure magnitudes at two span stations between the coupled CFD-beam simulation and experimental results showing reasonable agreement. The coupled CFD-beam results should be viewed mostly as an initial validation of our beam structural model, since in this case aeroelastic coupling is weak and similar results between prescribed modal motion and coupled aeroelastic simulations are expected.

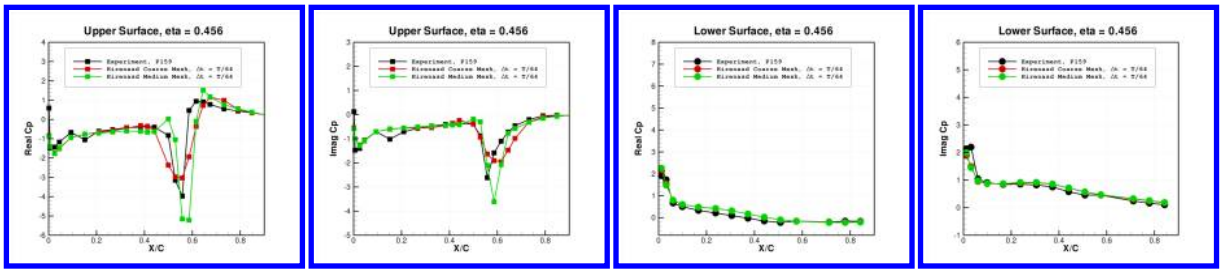

Figure 25. Comparison of computed versus experimental real and imaginary pressure fluctuations at y/b=0.456 station for HIRENASD with prescribed motion second-bending mode deflection at 78.9Hz.

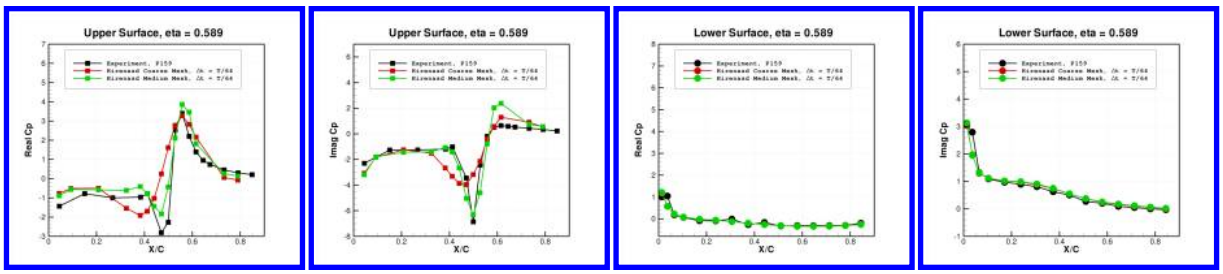

Figure 26. Comparison of computed versus experimental real and imaginary pressure fluctuations at y/b=0.589 station for HIRENASD with prescribed motion second-bending mode deflection at 78.9Hz.

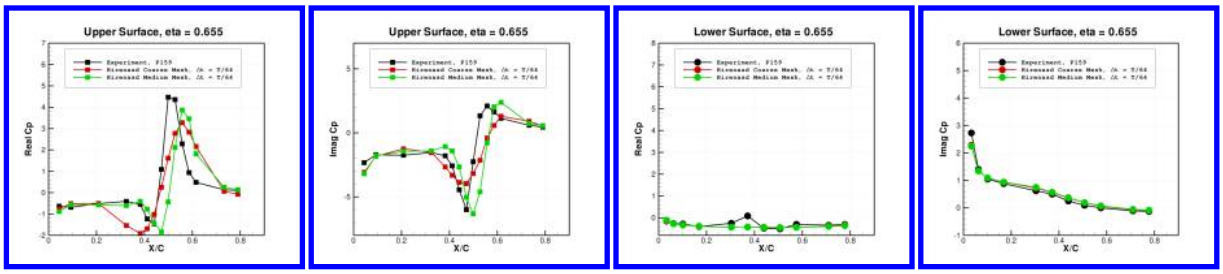

Figure 27. Comparison of computed versus experimental real and imaginary pressure fluctuations at y/b=0.655 station for HIRENASD with prescribed motion second-bending mode deflection at 78.9Hz.

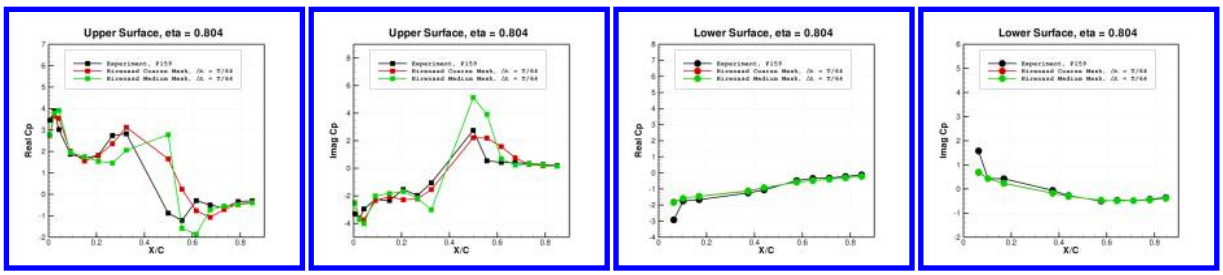

Figure 28. Comparison of computed versus experimental real and imaginary pressure fluctuations at y/b=0.804 station for HIRENASD with prescribed motion second-bending mode deflection at 78.9Hz.

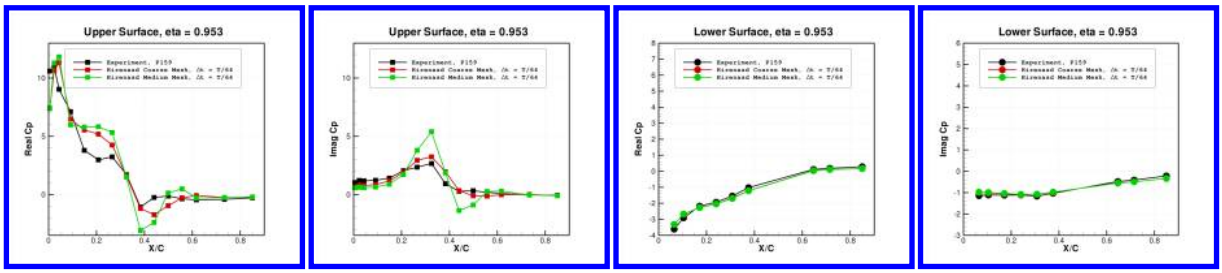

Figure 29. Comparison of computed versus experimental real and imaginary pressure fluctuations at y/b=0.953 station for HIRENASD with prescribed motion second-bending mode deflection at 78.9Hz.

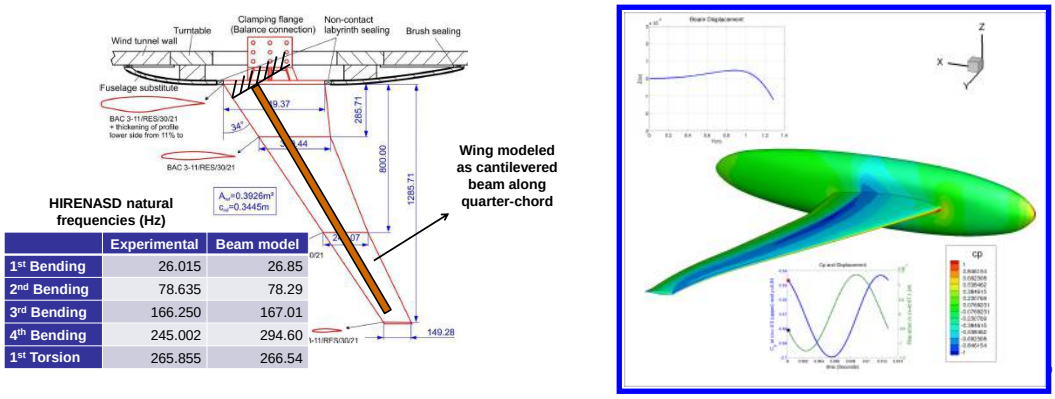

(a) (b)

Figure 30. (a) HIRENASD beam model configuration; (b) Sample coupled aeroelastic simulation using beam model.

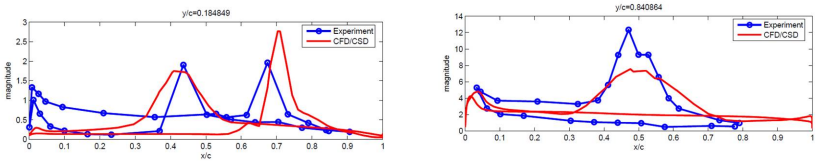

(a) y/b=0.145 (b) y/b=0.804

Figure 31. Comparison of computed versus experimental pressure fluctuation magnitude at y/b=0.145 and y/b=0.804 stations for HIRENASD fully coupled aeroelastic simulation using beam model.

VI. Summary and Future Work

Participation in the first aeroelastic workshop has provided a valuable exercise for benchmarking both unsteady aerodynamic and fully aeroelastic simulation capabilities. Such simulations are more complex than steady-state aerodynamic calculations since multiple disciplines must be linked together and can contribute various sources of errors.

The workshop results represent a large amount of data, particularly when grid refinement, time step refinement and convergence tolerance effects are included. Although the results described in this paper covered all three test cases from the workshop, for each test case, additional grid and time step refinement studies are warranted. For the RSW case, it was felt that better agreement with experiment should have been expected but that this was mostly due to the unexpected complications due to the interaction of the model with the wind-tunnel wall boundary layer. One suggestion was a CFD-only comparison of this same test case using a purely inviscid wall. The BSCW was designed as a challenging test case and will likely serve as a model for future investigations of strongly non-linear time-dependent flow phenomena which are known to be at the edge of the capabilities of current RANS solvers. One of the important outcomes of the results of this work was the demonstration of the need to resolve the important time scales of these flow phenomena simply for good implicit time-step convergence. Finally, the HIRENASD case provided a good entry-level test case for aeroelastic simulations and agreement with experimental data has been shown to be quite good in most regions of the flow field. Follow on work may involve investigating more non-linear aeroelastic responses and more highly coupled aeroelastic problems.

References

[1]Levy, D. W., Zickuhr, T., Vassberg, J., Agrawal, S., Wahls, R. A., Pirzadeh, S., and Hemsch, M. J., "Data Summary from the First AIAA Computational Fluid Dynamics Drag Prediction Workshop," *Journal of Aircraft*, Vol. 40, No. 5, 2003, pp. 875–882.

[2]Levy, D. W., Laflin, K. R., Vassberg, J. C., Tinoco, E., Mani, M., Rider, B., Brodersen, O., Crippa, S., Rumsey, C. L., Wahls, R. A., Morrison, J., Mavriplis, D. J., and Murayama, M., "Summary of Data from the Fifth AIAA CFD Drag Prediction Workshop," AIAA Paper 2013 to be presented at the 51st Aerospace Sciences Meeting, Grapevine TX.

[3]Benek, J. A., "Lessons learned from the 2010 AIAA Shock Boundary Layer Interaction Prediction Workshop," AIAA Paper 2010-4825.

[4]Rumsey, C. R., Long, M., Stuever, R. A., and Wayman, T. R., "Summary of the First AIAA High-Lift Prediction Workshop," AIAA Paper 2011-939 presented at the 49th AIAA Aerospace Sciences Meeting, Orlando FL.

[5]Mavriplis, D. J. and Levy, D. W., "Transonic Drag Prediction using an Unstructured Multigrid Solver," *AIAA Journal of Aircraft*, Vol. 42, No. 4, 2003, pp. 887–893.

[6]Lee-Rausch, E. M., Frink, N. T., Mavriplis, D. J., Rausch, R. D., and Milholen, W. E., "Transonic Drag Prediction on a DLR-F6 Transport Configuration using Unstructured Grid Solvers," *Computers and Fluids*, Vol. 38, No. 3, March 2009, pp. 511–532.

[7]Mavriplis, D. J., "Third Drag Prediction Workshop Results using the NSU3D Unstructured Mesh Solver," *AIAA Journal of Aircraft*, Vol. 45, No. 3, May 2008, pp. 750–761.

[8]Mavriplis, D. J. and Long, M., "NSU3D Results from the Fourth AIAA CFD Drag Prediction Workshop," AIAA Paper 2010-4364.

[9]Long, M. and Mavriplis, D. J., "NSU3D Results from the First AIAA CFD High-Lift Prediction Workshop," AIAA Paper 2011-863 presented at the 49th AIAA Aerospace Sceinces Meeting.

[10]Mavriplis, D. J., "Grid Resolution Study of a Drag Prediction Workshop Configuration Using the NSU3D Unstructured Mesh Solver," AIAA-Paper 2005-4729.

[11]Sitaraman, J., Wisssink, A., Sankaran, V., Jayaraman, B., Datta, A., Yang, Z., Mavriplis, D., Saberi, H., Potsdam, M., O'Brien, D., Cheng, R., Hariharan, N., and Strawn, R., "Application of the HELIOS Computational Platform to Rotorcraft Flowfields," AIAA Paper 2010-1230, Presented at the 48th AIAA Aerospace Sciences Meeting, Orlando FL.

[12]Mavriplis, D. J. and Venkatakrishnan, V., "A Unified Multigrid Solver for the Navier-Stokes Equations on Mixed Element Meshes," *International Journal for Computational Fluid Dynamics*, Vol. 8, 1997, pp. 247–263.

[13]Spalart, P. R. and Allmaras, S. R., "A One-equation Turbulence Model for Aerodynamic Flows," *La Recherche Aérospatiale*, Vol. 1, 1994, pp. 5–21.

[14]Wilcox, D. C., "Re-assessment of the scale-determining equation for advanced turbulence models," *AIAA Journal*, Vol. 26, 1988, pp. 1414–1421.

[15]Menter, F. R., "Two-Equation Eddy-Viscosity Turbulence Models for Engineering Applications," *AIAA Journal*, Vol. 32, No. 8, 1994, pp. 1598–1605.

[16]Mavriplis, D. J. and Yang, Z., "Construction of the Discrete Geometric Conservation Law for High-Order Time Accurate Simulations on Dynamic Meshes," *Journal of Computational Physics*, Vol. 213, No. 1, April 2006, pp. 557–573.

[17]Yang, Z. and Mavriplis, D. J., "High-Order Time Integration Schemes for Aeroelastic Applications on Unstructured Meshes," *AIAA Journal*, Vol. 45, No. 1, 2007, pp. 138–150.

[18]Yates, E. C. J., "AGARD Standard Aeroelastic Configurations for Dynamic Response I - Wing 445.6," Tech. Rep. TM 100492, NASA, 1987.

[19]Sitaraman, J., Datta, A., Baeder, J., and Chopra, I., "Coupled CFD/CSD Prediction of Rotor Aerodynamic and Structural Dynamic Loads for Three Critical Flight Conditions," 31st European Rotorcraft Forum, Florence, Italy.

[20]Datta, A., Sitaraman, J., Baeder, J., and Chopra, I., "CFD/CSD Prediction of Rotor Airloads in High Speed Flight," *Journal of Aircraft*, Vol. 43, No. 6, 2006, pp. 1698–1709.

[21]Sitaraman, J. and Roget, B., "Prediction of Helicopter Maneuver Loads using a Fluid/Structure Analysis," *Journal of Aircraft*, Vol. 46, No. 5, 2006, pp. 1770–1784.

[22]Yang, Z. and Mavriplis, D. J., "A Mesh Deformation Strategy Optimized by the Adjoint Method on Unstructured Meshes," *AIAA Journal*, Vol. 45, No. 12, 2007, pp. 2885–2896.

[23]Ricketts, R. H., Sanford, M. C., Seidel, D. A., and Watson, J. J., "Transonic Pressure Distributions on a Rectangular Supercritical Wing Oscillating in Pitch," *AIAA Journal of Aircraft*, Vol. 21, No. 8, 1983, pp. 576–582.

[24]Schuster, D. M., Chwalowski, P., Heeg, J., and Wieseman, C. D., "Summary of Data and Findings from the First Aeroelastic Prediction Workshop," Paper ICCFD7-3101, Proceedings of the 7th ICCFD Conference, Mauna Lani Bay Hawaii.

[25]Ballmann, J., Dafnis, A., Korsch, H., Buxel, C., Reimerdes, H. G., Brakhage, K. H., Olivier, H., Braun, C., Baars, A., and Boucke, A., "Experimental Analysis of High Reynolds Number Aero-Structural Dynamics in ETW," AIAA Paper 2008-841.

[26]Reimer, L., Boucke, A., Ballmann, J., and Behr, M., "Computational Analysis of High-Reynolds Number Aero-structural dynamics HIRENASD," Proc. of the International Forum on Aeroelasticity and Structural Dynamics (IFASD) 2009, Paper IFASD-2009-130.